Ocean Modelling 29 (2009) 198–212

Contents lists available at ScienceDirect

Ocean Modelling

journal homepage: www.elsevier.com/locate/ocemod

Sensitivity of mixed layer heat budgets to wind forcing: A case study for the equatorial Pacific cold tongue

Sophie Cravatte [a,b,*], Christophe Menkes [c]

[a] Université de Toulouse, UPS (OMP-PCA), LEGOS, 14 Avenue Edouard Belin, F-31400 Toulouse, France
[b] IRD, LEGOS, F-31400 Toulouse, France
[c] IRD, LOCEAN, UMR IRD/MNHN/CNRS/UPMC, IRD, BP A5, 98848 Nouméa, New Caledonia

ARTICLE INFO

Article history:
Received 27 November 2008
Received in revised form 30 March 2009
Accepted 26 April 2009
Available online 5 May 2009

Keywords:
Equatorial Pacific cold tongue
Mixed layer heat budget
Ocean General Circulation Model
Wind forcing

ABSTRACT

Ocean General Circulation Models (OGCMs) are very useful tools to analyze and quantify heat budget terms governing the sea surface temperature variability. However, model results are strongly dependant on the momentum forcing used. In this study, five simulations of a climate-type OGCM, forced by different wind stress products from atmospheric reanalyses, satellites and *in situ* data are performed. They are analyzed in the eastern tropical Pacific from 1993 to 2000, in the Pacific cold tongue, a key region where all terms of the heat budget are important. The differences in thermodynamical and dynamical oceanic parameters relevant for mixed layer budgets are first documented in the five simulations, and validations against observations are presented at annual and intraseasonal scales. It is then shown that the different components of the oceanic heat budget are quantitatively greatly affected by the choice of the wind forcing, and the amplitude of the terms explaining sea surface temperature variations can double from one simulation to the other. In contrast, the relative contributions of the terms, i.e. mean advection, atmospheric forcing, mixing at the base of the mixed layer and contributions of eddies are the same in all simulations forced by different wind stress products. This is true for the mean 1993–2000 period, at seasonal timescales and during interannual events such as the abrupt cooling observed in the cold tongue in May 1998. This paper thus suggests that model users can be confident in the physical processes governing sea surface temperature variability whatever the wind stress used to force their model is, but they must be very cautious when estimating quantitatively heat budgets terms with one simulation only.

© 2009 Elsevier Ltd. All rights reserved.

1. Introduction

The equatorial Pacific cold tongue is a conduit with continuous mass and heat exchanges. It is characterized by surface current divergence and upwelling. The thermocline there is close to the surface, and the strong vertical stratification leads to a thin mixed layer. It is an oceanic region with one of the most intense heat gain from the atmosphere, and a key region for the ENSO (El Niño-Southern Oscillation) phenomenon. Understanding the oceanic processes that redistribute the atmospheric flux entering the ocean, and drive sea surface temperature (SST) variability on annual and interannual scales is fundamental.

Motivated by this important issue, several empirical (Stevenson and Niiler, 1983; Bryden and Brady, 1985, 1989; Enfield, 1986; Hayes et al., 1991; Swenson and Hansen, 1999; Wang and McPhaden, 1999, 2000, 2001a) and numerical (Kessler et al., 1998; Vialard et al., 2001; Menkes et al., 2006; Jochum and Murtugudde, 2006; Kim et al., 2007) studies examined the mean heat budget in the region, as well as its seasonal and interannual variability. Using meridional hydrographic sections, Bryden and Brady (1985) determined the heat budget for the 150–110°W, 5°S–5°N box. This pioneering work showed that the heat gain from the atmosphere was redistributed westward and poleward by surface currents and that strong upwelling contributed to maintain the cold tongue. Subsequent papers confirmed and detailed these findings. Basically, upwelling brings cold water up to the near-surface, turbulence entrainment flux brings it into the cold tongue and the surface Ekman divergence then exports it from the cold tongue poleward, while atmospheric fluxes and zonal and meridional eddy advection warm the cold tongue.

Eddies at 15–45 day-periods also contribute to the warming and are associated with tropical instability waves (TIW). TIW are large-scale westward-propagating perturbations of currents and temperature, often observed as meanders in the front separating cold waters of the equatorial upwelling from warmer waters to the north (Legeckis, 1977). Observed in the 10–50 days period

* Corresponding author. Address: Université de Toulouse, UPS (OMP-PCA), LEGOS, 14 Avenue Edouard Belin, F-31400 Toulouse, France. Tel.: +33 5 61 33 30 05; fax: +33 5 61 25 32 05.
E-mail addresses: Sophie.Cravatte@ird.fr (S. Cravatte), Christophe.Menkes@noumea.ird.nc (C. Menkes).

1463-5003/$ - see front matter © 2009 Elsevier Ltd. All rights reserved.
doi:10.1016/j.ocemod.2009.04.005

band, they can be separated into an equatorial and off-equatorial signal. The equatorial signal peaks at 17-day in observations and may be described as Yanai waves (Lyman et al., 2005). The signal that is found north of the equator has a broader frequency peak centred at about 30 days and may be interpreted as a combination of the equatorial signal, Rossby waves (Lyman et al., 2005) and other dynamical processes. It can also be viewed as nonlinear westward moving eddies or tropical instability vortices (Dutrieux et al., 2008; Kennan and Flament, 2000; Menkes et al., 2002; Menkes et al., 2006). Their complex three-dimensional structure strongly modulates the SST field at intraseasonal timescale. Since the initial suggestion of eddy-induced warming (Hansen and Paul, 1984), considerable efforts have been made to precisely quantify the eddies heat advection in observations and model studies (Baturin and Niiler, 1997; Vialard et al., 2001; Jochum and Murtugudde, 2006; Menkes et al., 2006; Jochum et al., 2007; Dutrieux et al., 2008).

At seasonal timescales, the SST variations have also been attributed to a variety of processes (Enfield, 1986; Kessler et al., 1998; Swenson and Hansen, 1999; Wang and McPhaden, 1999, 2001b). The equatorial upwelling, turbulent entrainment and eddy heat fluxes, that mimic the mean seasonal cycle of surface winds, are strongest during the second half of the year. Their variations tend to cancel each other, and the SST variations finally appear to follow the variation of net solar radiation at the ocean surface (Kessler et al., 1998). During an El Niño event, oceanic processes drive SST changes, while atmospheric processes restrain them (Hayes et al., 1991; Wang and McPhaden, 2000; Vialard et al., 2001; Boulanger and Menkes, 2001; Kim et al., 2007), together with the reduction of warming due to weakened TIWs. Anomalous zonal advection of warm waters from the west, weakening of vertical turbulent mixing and entrainment have all been suggested to contribute to the warming of the cold tongue.

Thus, the heat budget of the cold tongue has been largely studied. The conclusion is that it is a very complex region where all different terms may significantly contribute to the heat budget, at one time or another. A major remaining uncertainty concerns the quantitative estimation of the different terms. In particular, the magnitude of cooling by vertical processes and warming by eddy-advection which partitions into zonal, meridional and vertical contributions are still an object of active research. It is quite unachievable to close heat budgets and to accurately compute these components of the mixed layer tendency budget with observations. Models can help in this purpose. However, the problem with model results is that they may be sensitive to the model physics, including mixed layer physics, lateral diffusion parameterizations (Jochum et al., 2005; Menkes et al., 2006) and, perhaps more importantly, to the atmospheric forcing used to force these models.

Different wind stress products are available to force OGCMs, and these wind stress products have different spatial and temporal resolutions, and different amplitudes. It is well known that, in the equatorial region particularly, momentum forcing can vary widely depending on the data set chosen (e.g. Busalacchi et al., 1993; Liu et al., 1996; Fu and Chao, 1997; Grima et al., 1999; Milliff et al., 1999; Hackert et al., 2001). The equatorial model dynamics is dominated by and is sensitive to the choice of the wind stress forcing used (Liu et al., 1996; Hackert et al., 2001; Agarwal et al., 2007; Jiang et al., 2008; Athie et al., submitted for publication) although heat fluxes may play a secondary role (Ayina et al., 2006). Differences in the wind forcing affect the surface and subsurface dynamics and thermodynamics, and the depth of the mixed layer. Liu et al. (1996) and Ayina et al. (2006) also suggested that they affect the different components of the oceanic heat budget, but they only touched briefly upon this subject.

The previous studies cited above have often used the response of ocean models as a way to evaluate a particular wind stress, whether it is a satellite wind or a reanalysis wind. Here, we wish to build on these previous studies not to assess a "best wind stress product" but rather to evaluate incertitude for mixed layer heat budgets in an OGCM and determine what robustness is expected from model results. Are the relative contributions of TIWs, mean advection, atmospheric forcing and mixing at the base of the mixed layer changed in simulations with different wind forcings? Are they similar during particular periods such as abrupt coolings during the transition from El Niño to La Niña? Then, what can be our confidence in heat budgets performed with one wind forcing or another? Quantitatively? Qualitatively?

The paper is organized as follows. Section 2 presents the model and the wind products used to force it. Section 3 briefly presents the differences in the model simulations in dynamics and thermodynamics oceanic fields that matter to explain the heat budget. Section 4 compares the contribution of the components of the 1993–2000 mean and of the mean seasonal mixed layer heat budget in the different simulations. The comparison is also done during one particular event (the abrupt cooling during the transition phase from El Niño to La Niña in May 1998). Section 5 concludes and discusses our result implications.

2. Model and forcings

2.1. Model description

The OGCM used in this study is the OPA model (Madec et al., 1998) in its global configuration ORCA2. This configuration is used for a wide range of oceanographic and climatic studies, notably used for IPCC (Intergovernmental Panel on Climate Change). The horizontal mesh is based on a 2° by 2° Mercator grid. In addition, the meridional resolution is enhanced in the tropics, reaching up to 0.5° in latitude at the equator. There are 31 vertical levels from surface to bottom with a resolution of 10 m in the upper 150 m, decreasing to 500 m in the deep ocean. The model uses a free surface formulation (Roullet and Madec, 2000). Lateral tracer and momentum mixing is done along isopycnals, as it has been shown that this parameterization is best suited to simulate the observed eddy effects in the tropics (Lengaigne et al., 2003; Pezzi and Richards, 2003). Vertical eddy viscosity and diffusivity coefficients are computed from a 1.5 turbulent closure scheme based on a prognostic equation for the turbulent kinetic energy (Blanke and Delecluse, 1993) and a diagnostic equation for the dissipation and the mixing turbulent length scales. A flux corrected transport (FCT) advection scheme (Zalesak, 1979) described and tested in (Levy et al., 2001) is used, instead of the second order centered advection scheme usually used in OPA. More details about this configuration can be found in (Cravatte et al., 2007).

The momentum forcing of the model comes from 1993 to 2000 different wind stresses (see next paragraph). To limit our sensitivity study to momentum forcing, heat and freshwater fluxes are all computed using semi empirical and bulk formulae (Goose, 1997) with the same input files: precipitations are taken from observations (Xie and Arkin, 1996) and other atmospheric forcing fields consist of the NCEP/NCAR daily reanalysis data of surface air temperature and relative humidity, cloudiness and 10 m wind speed (Kalnay et al., 1996). Let us stress that modelled SSTs enter the flux calculation, thus there is an indirect sensitivity of the heat and freshwater fluxes to the different stresses but it is believed to be limited especially because such flux formulation also introduces a sort of relaxation term of SST towards the NCEP SST through the turbulent fluxes. Moreover, it implies that differences in ocean thermodynamics and dynamics we will observe will be attribut-

Table 1
Description of the different wind stress products used to force the OGCM before being interpolated onto the model grid.

	Spatial resolution (latitude by longitude)	Temporal resolution	Source
RUN-ERS	1° by 1°	7 days	CERSAT-IFREMER
RUN-TAO	1° by 1°	5 days	Menkes et al. (1998)
RUN-SSMI	1° by 1°	5 days	Atlas et al. (1999)
RUN-NCEP	1.875° by 1.915°	Daily	NCEP1; Kistler et al. (2001)
RUN-ERA	1.125° by 1.125°	Daily	ERA-40; Uppala et al (2005)

able to differences in wind stress only. The solar radiation penetrates the top meters of the ocean, with a downward irradiance formulated with two extinction coefficients (Paulson and Simpson, 1977) whose values correspond to a type I water in Jerlovs classification. The model starts from an ocean at rest with January temperature and salinity fields from the Levitus (1998) climatology. It is spun up for a 3-year period using 1993 forcing fields before starting the interannual simulations. Daily outputs are provided.

2.2. Wind forcings

Five different wind stresses are used to force the OGCM, originating from satellite and in situ data as well as from reanalysis products. The first wind stress field (RUN-ERS forcing) is obtained from ERS-1 and ERS-2 scatterometer data (Bentamy et al., 1996). The second 5-day product, (RUN-TAO forcing), is obtained from wind stresses derived by combining ERS-1 and ERS-2 scatterometer data with the in situ TAO data, with a smoothed transition to NCEP wind stresses poleward of 60° (Menkes et al., 1998, 2006). The third one is obtained from SSMI/I wind (RUN-SSMI forcing). 5 day average SSM/I wind data from (Atlas et al., 1999) are converted into stress using a constant 1.2 E^{-3} drag coefficient. The two other wind-forcing fields are the daily NCEP/NCAR wind stresses (Kistler et al., 2001) (RUN-NCEP forcing) and the daily ERA-40 reanalysis wind stresses (Uppala et al., 2005) (RUN-ERA forcing). These five wind stress products have different original spatial and temporal resolutions (Table 1), and they have all been interpolated onto the model grid.

Mean 1993–2000 zonal wind stresses and mean wind stress curls are shown in Fig. 1, and Table 2 summarizes information about the mean and the standard deviation of the different products. Obviously, intensities of the mean zonal wind stresses are

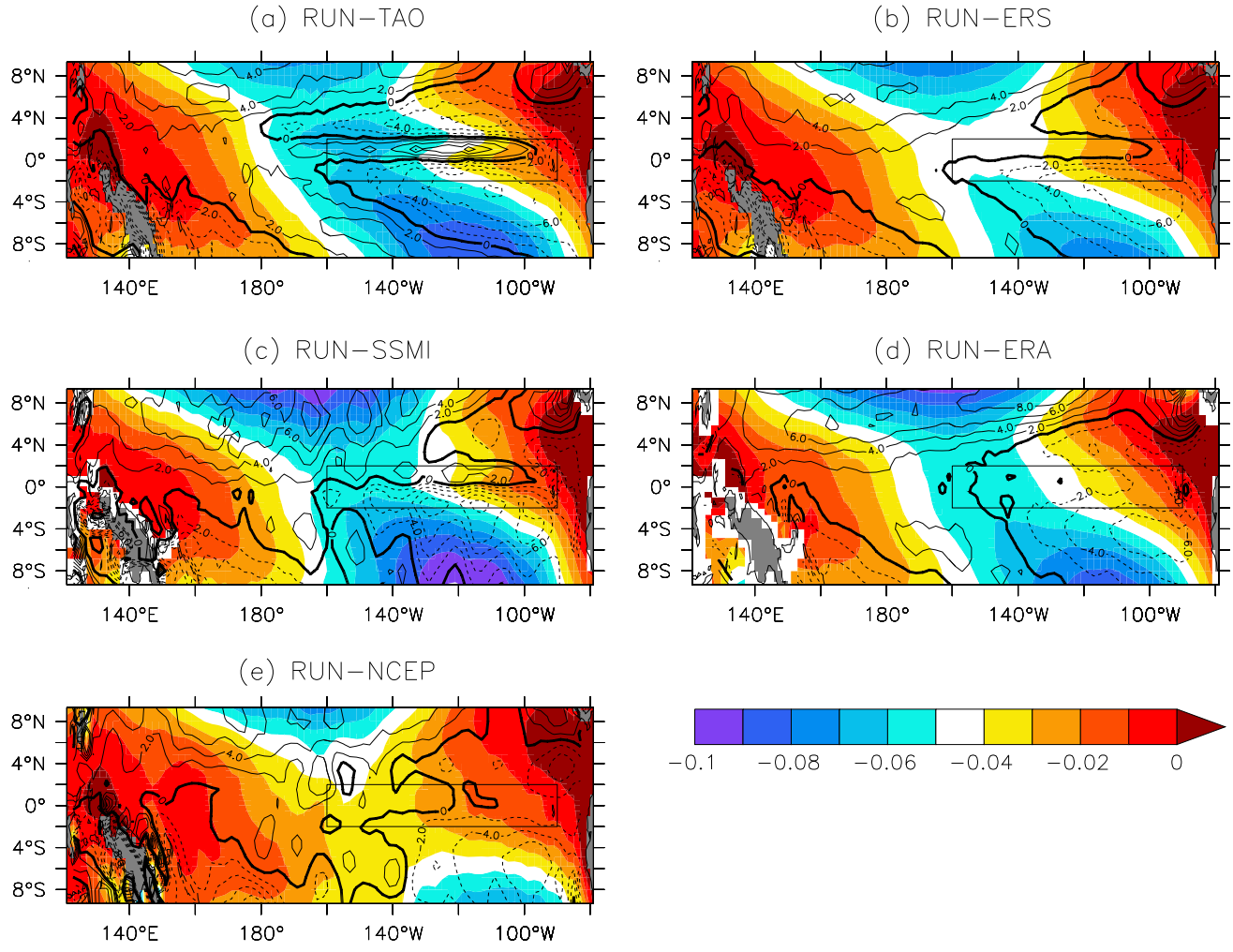

Fig. 1. Zonal wind stress (colors) in N m^{-2} and wind stress curl (contours) in 10^{-8} N m^{-2} from the five simulations. Contours are plotted every 2×10^{-8} N m^{-2}. The boxes represent the 160–90°W, 2°S–2°N region.

Table 2
Properties of the different wind stress products interpolated onto the model grid, for the January 1993 to December 2000 period. The mean and the standard deviation (STD) of the zonal wind stress are in 10^{-2} N m^{-2}, and the mean kinetic energy input (KE) in the ocean per unit area (see text) is in W m^{-2}.

	RUN-ERS	RUN-TAO	RUN-SSMI	RUN-ERA	RUN-NCEP
Mean zonal wind stress, 2°S–2°N, 120°E–80°W	−2.27	−3.04	−2.66	−2.76	−1.75
Mean zonal wind stress, 2°S–2°N, 160–90°W	−3.34	−4.43	−4.10	−4.04	−2.55
Interannual STD of the zonal wind stress, 2°S–2°N, 120°E–80°W	1.0	1.5	1.3	1.1	0.8
Seasonal STD of the zonal wind stress, 2°S–2°N, 120°E–80°W	0.7	1.0	0.9	0.9	0.6
Intraseasonal STD of the zonal wind stress, 2°S–2°N, 120°E–80°W	1.4	1.8	1.7	2.0	1.6
KE input, 10°S–10°N, 120°E–80°W	0.53	0.92	0.84	0.80	0.35
KE input, 2°S–2°N, 160–90°W	1.25	2.25	1.59	2.17	1.17

quite different in the five products. As already noticed by Menkes et al. (1998), the RUN-TAO forcing is stronger than the RUN-ERS forcing. RUN-SSMI and RUN-ERA are close and weaker than RUN-TAO at the equator, but stronger poleward of 5°. NCEP zonal wind stress is notably weaker as already noted (Agarwal et al., 2007). Interestingly, the reanalyses fail to reproduce the narrow strip of positive curl along the SST front just north of the equator from about 160° to 100°W (Fig. 1d and e), which is clearly visible in RUN-ERS, RUN-SSMI, and especially in RUN-TAO fields (Fig. 1a). This pattern is also visible in QuikSCAT winds as shown in Kessler et al.'s (2003) Fig. 5. Its strength in the TAO wind field is obviously overestimated compared to the satellite data and that is probably due to the paucity of TAO buoy meridional positions at equator, 2 and 5°N. This small feature has been suggested to be important for Sverdrup-derived zonal currents (Kessler et al., 2003). Failure to represent that feature in the reanalyses might be in part explained by the poor meridional resolution, especially in the NCEP wind. More probably, it may be the atmospheric model dynamics itself that lead to missing that feature, despite the satellite data assimilation.

Another interesting wind characteristic useful for the oceanic response is the wind kinetic energy input (KE) in the ocean. Defined as the dot product of wind stress and surface current, it represents the mechanical wind energy input into the ocean. In the tropical Pacific, one of the main source of KE for the global ocean, it depends mainly onto the wind stress strength and the structure of the simulated SEC (South Equatorial Current, where there is a transfer of energy into the ocean) and of the NECC (North Equatorial CounterCurrent, where there is a removal of energy from the ocean) (Brown and Fedorov, 2008). As can be seen in Table 2, the KE into the ocean is greater for RUN-TAO, important for RUN-SSMI and RUN-ERA, lower for RUN-ERS and much lower for RUN-NCEP. These differences may in particular affect the mean thermocline slope and the turbulent kinetic energy dissipated in the mixed layer.

Finally, standard deviations at seasonal, intraseasonal and interannual timescales are compared (Table 2). At seasonal and interannual timescales, RUN-TAO zonal wind stress forcing exhibits the highest variability in the equatorial band and RUN-NCEP the lowest. At intraseasonal timescales, RUN-ERA zonal wind stress forcing exhibits the highest variability because of its daily resolution, and RUN-ERS the lowest. Determining how such variability impacts the oceanic variability is absolutely not straightforward in a nonlinear complex OGCM as the following will show.

3. Differences in oceanic temperature, current and eddy fields

The differences in intensity, frequency and variability of wind stress products create important differences in surface and subsurface dynamical and thermodynamical ocean responses. For the sake of this paper, we will not describe all the differences induced by these various wind forcings, but rather will focus on the ocean parameters relevant for mixed layer budgets.

3.1. Mean temperature

The mean 1993–2000 modelled temperatures are first validated against Reynolds and Smith's (1994) data and TAO/TRITON moorings in situ temperatures. Typical mean simulated SSTs are shown in Fig. 2b, and are closed to the observed ones (Fig. 2a). In our model simulations, there is no hint of the cold bias that has been reported in previous studies (Karnauskas et al., 2007) even with the five different wind products. Different wind forcing products lead to different mean SSTs in the cold tongue region indicating different heat budget equilibrium. The RUN-SSMI is colder and closer to the observations than the other runs (Fig. 2c). The RUN-NCEP is warmer in the whole equatorial band. Despite the underlying relaxation toward NCEP air surface temperature exerted by the turbulent fluxes on SST, there is as much as 1.8 °C difference in the cold tongue region between RUN-SSMI and RUN-NCEP. The meridional SST gradients are identical (not shown), and the zonal SST gradients in the five runs are similar. It is slightly greater in SSMI-RUN and close to the observations, and weaker in NCEP-RUN. There are also differences in the eastern part of the cold tongue, with SSMI-RUN exhibiting a stronger positive SST zonal gradient. Nevertheless, these differences are small and their impact on the mean zonal advection will be negligible.

At depth, the thermocline is too diffuse in all the runs (not shown), a well-known bias for ocean models in the equatorial region (see, for example Jiang et al.'s (2008) Fig. 4a for another ocean model example). The mean depth and zonal slope of the thermocline almost directly depend on the zonal wind stress, and more precisely on the wind kinetic energy input, as suggested by Brown and Fedorov (2008). In RUN-NCEP, because of the wind weakness, the thermocline is too shallow in the western equatorial Pacific and too deep in the eastern part of the basin. In the other runs, the mean depth and the mean thermocline slope are much more realistic and close to the observed ones, with slight differences between the runs linked to the wind kinetic energy input differences (see Table 2).

3.2. Mean surface and subsurface equatorial currents

The mean 1993–2000 modelled surface currents are also validated against a drifter-derived climatology of global near-surface currents representative of about the same time period, kindly provided by Dr. Lumpkin (Lumpkin and Garraffo, 2005). That climatology is essentially representative of the 1992-present period (Lumpkin, personal communication).

The two branches of the westward SEC, the eastward NECC, and a part of the weak eastward South Equatorial CounterCurrent are correctly captured in all runs (Fig. 3). However, the intensity of the two branches of the SEC and of the NECC is dependent onto the wind forcing. North of the equator, the SEC is too weak in virtually all runs as compared to the Lumpkin's observations (see also Fig. 4b). However, independent observations from TAO equatorial moorings at 140 and 110°W suggest different conclusions. Indeed,

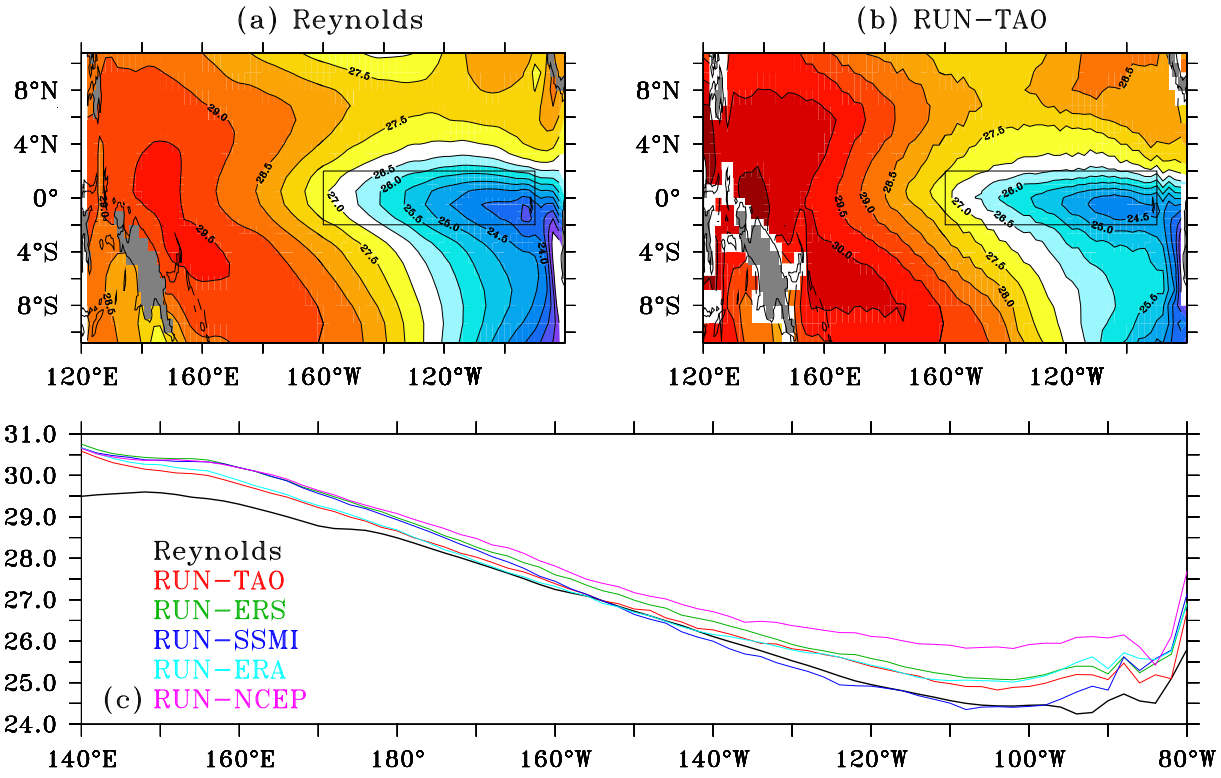

Fig. 2. (a) Mean 1993–2000 Reynolds SST. (b) Mean 1993–2000 SST for RUN-TAO. The boxes represent the 160–90°W, 2°S–2°N region. (c) Mean 1993–2000 SST averaged in the 2°S–2°N latitudinal band from Reynolds data (thick black line) and from the five simulations. Units are °C.

simulated zonal currents extracted at the TAO mooring locations at every time step where data are available during the 1993–2000 period indicate that the modelled SEC is too strong compared to the observations (see also Fig. 5). This suggests that the drifter climatology may overestimate the mean zonal current by more than 20 cm s^{-1}. Mean TAO equatorial zonal currents at 110 and 140°W are 8 and −11 cm s^{-1}, respectively while the drifter estimate are 6 and −23 cm s^{-1}, respectively. It is difficult though to compare the drifter climatology with TAO currents at precise locations, since the drifter climatology is very noisy at the equator, and the exact period represented by drifter data in the climatology is not well defined. Moreover, drifters tend to move away from divergence areas such at the equator, thus lower sampling and less robustness is found in that area. All things considered, that inconsistency between Lumpkin's and TAO data prevents us from drawing firm conclusions on the simulated SEC intensity right at the equator. Finally, the SEC minimum and the southern branch of the SEC are also not very well simulated as these are shifted to the north in the model runs as shown in Figs. 3 and 4b.

The case of the NECC is interesting in that the two satellite-derived products (SSM/I and ERS) give simulations with very unrealistic NECC, especially in the western Pacific, with a southward bifurcating NECC off 140°E. While we do not expect to catch the right variability near the western boundary in the Mindanao region – due to low spatial resolution- the behaviour of these satellite wind forced simulations in the NECC is puzzling. Sensitivity studies performed in other conditions with the other OGCM ROMS (Regional Ocean Model System) (Shchepetkin and McWilliams, 2005) for ERS and QuikSCAT forcing also exhibit very similar behaviour in the western Pacific. Hence, we think that it is the satellite forcing as provided that create these patterns. It is possible that rain-contaminated cells induce spurious data in this region of heavy convection but further studies need to be conducted to conclude about these problems (Zuojun Yu, personal communication).

Fig. 4 shows the 160–90°W zonal mean of the 15-m currents as a function of latitude. The 15-m flow is dominated by Ekman meridional currents that transport surface water away from the equator in both hemispheres, and by a strong upwelling. It appears that the mean structure and amplitude of the poleward currents are well captured in RUN-TAO and RUN-SSMI (Fig. 4a). They are slightly too weak in RUN-ERS and RUN-ERA, and markedly underestimated in RUN-NCEP. Similarly, the vertical velocity averaged in the 2°S–2°N band is 50% greater in RUN-SSMI and in RUN-TAO than in the weakest RUN-NCEP (Fig. 4c). This appears to be linked to the mean zonal wind stress differences, as Ekman surface divergence and upwelling are directly related to the zonal wind stress. These differences are consistent with properties of the wind stress products given in Table 2. Things are more complex for the 15-m zonal currents (Fig. 4b), which are generated by interplay of wind stress, wind curl and nonlinear dynamics, and an analysis of the momentum equations would be required to understand the structure differences.

Finally, the simulated currents of the five experiments are compared to TAO data. At 140 and 110°W, ADCP (Acoustic Doppler Current Profilers) and/or mechanical current meter are deployed and measure ocean currents down to 300 m at the equator. Owing to instrumental failure, the time series have missing values at some times and depths. Gaps are filled whenever possible using regression relations based on data from adjacent depths, and vertical spline interpolations are performed (as in Izumo (2005)). Finally, the daily current data are averaged into 5-day bins, and the simulated zonal currents are extracted at the TAO mooring locations at every time step where data are available during the 1993–2000 period (as Cravatte et al., 2007). The resulting mean vertical profiles of the TAO and simulated zonal currents at 140 and 110°W in Fig. 5 show the Equatorial UnderCurrent (EUC) structure down to 220 m, for the different experiments.

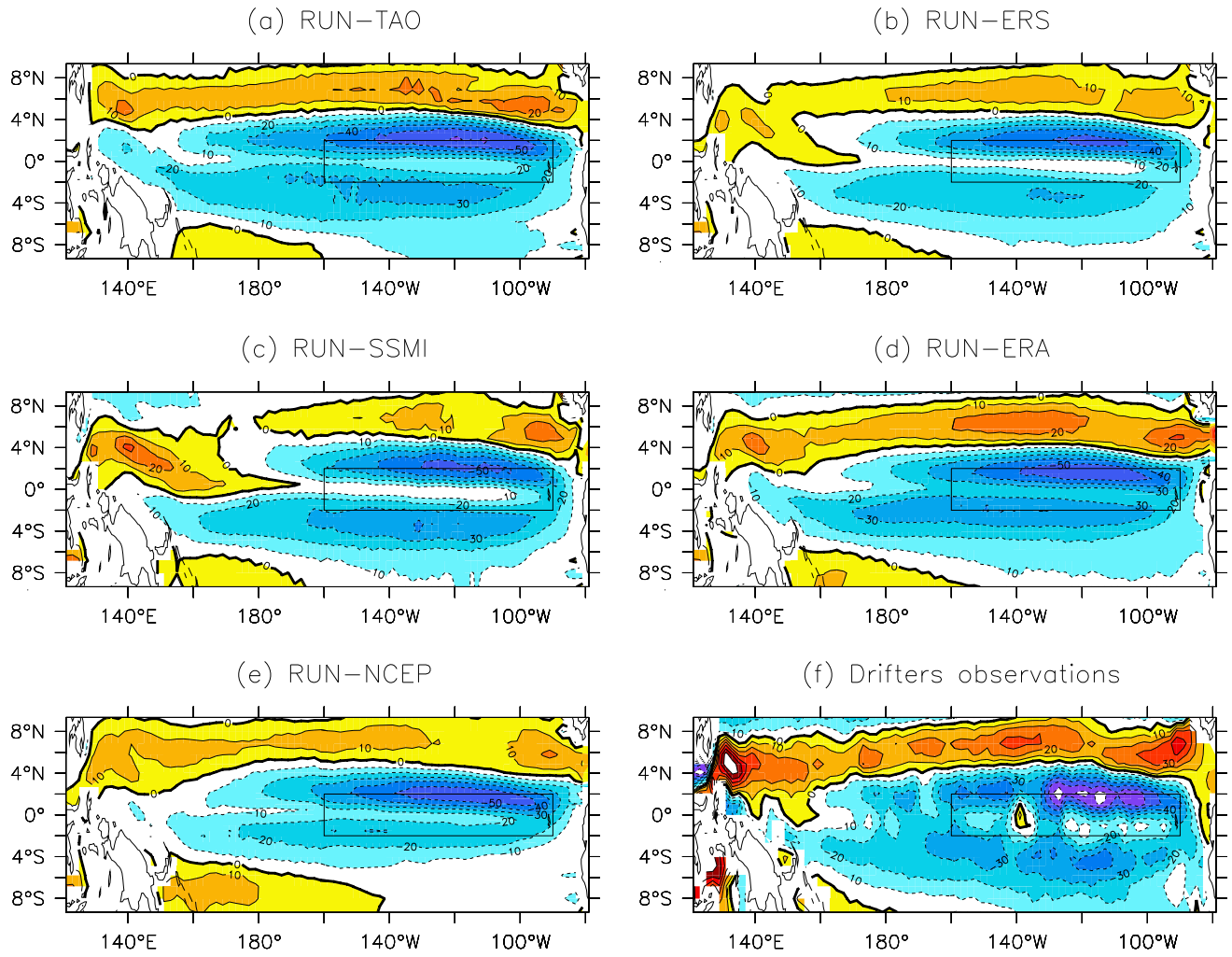

Fig. 3. Mean 1993–2000 zonal current at 15 m depth from Lumpkin's drifters observations (*f*) and from the five simulations. Units are cm s^{-1}. Contours are every 10 cm s^{-1}. The boxes represent the 160–90°W, 2°S–2°N region.

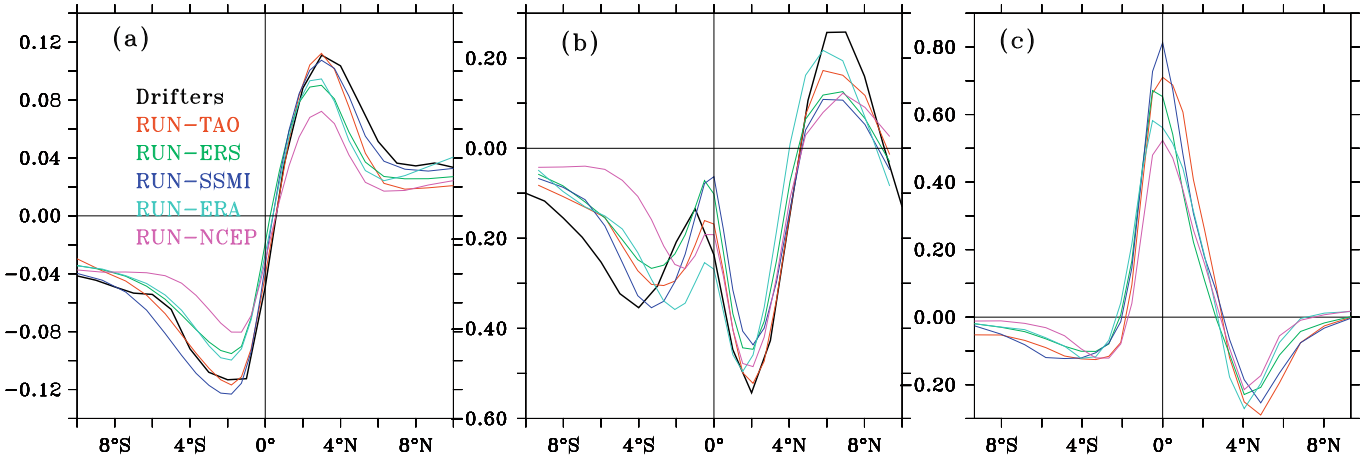

Fig. 4. Mean latitudinal section of (a) 15-m meridional velocity and (b) 15-m zonal velocity averaged in the 160–90°W box from Lumpkin's drifters observations (thick black line) and from the five simulations. Units are cm s^{-1}. (c) Mean latitudinal section of 15-m vertical velocity averaged in the 160–90°W box from the five simulations. Units are m day^{-1}.

It appears that the mean zonal current vertical structure is well captured by the five simulations. Important differences induced by the different choices of wind forcing can be observed in the intensity and in the depth of the EUC. The wind products that lead to the most realistic mean modelled EUC are the TAO and the ERA winds. In the RUN-NCEP, the strength of the EUC is highly underestimated at 140 and 110°W, and the core of the simulated EUC is shallower than in reality. In the RUN-SSMI and RUN-ERS, the depth of the EUC core is not well positioned.

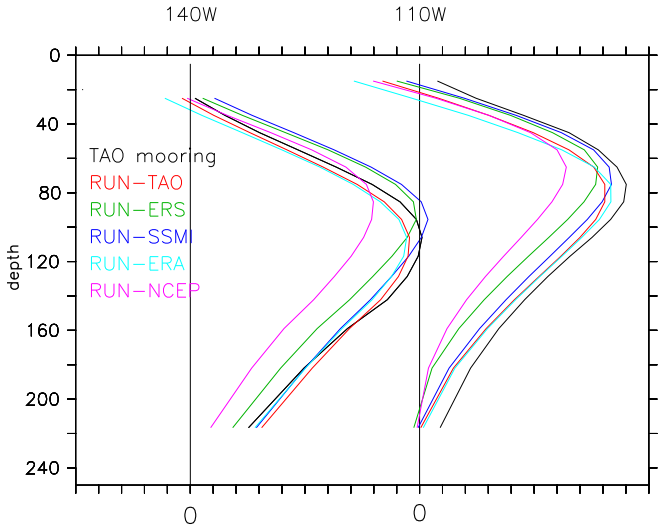

Fig. 5. Mean 1993–2000 zonal current profiles of TAO data (thick line) and of the five simulations. Comparisons at two moorings located in the cold tongue (140 and 110°W). Units are cm s^{-1}, and a tic represents 10 cm s^{-1}.

3.3. Tropical instability waves

To characterize the level of activity of the TIWs (equally referred to as "eddies" in the following) in our simulations, we use a time varying index similar to the one used in Vialard et al. (2003). It is estimated by taking the spatial root-mean square of the high-pass filtered SST over the 0–4°N, 160–90°W region. Data are filtered with a 69-day high-pass Sparzen filter to encompass all the observed frequencies. It is high when the box is occupied by large amplitude oscillation patterns. Fig. 6 shows this index for the five simulations and for SST data from the Tropical Rainfall Measuring Mission (TRMM) Microwave Imager (TMI) (Wentz et al., 2000) available from 1998. As expected, the level of TIWs activity is seasonally higher in boreal summer and autumn, higher during La Niña in 1998/1999 and lower during El Niño in 1997. It is known indeed that TIWs depend onto the mean background flow of the Tropical Pacific Ocean. Stronger in boreal autumn and winter, their intensity is greatly reduced during El Niño years (Contreras, 2002). It is greatly reliant on the wind forcing strength via a complex interaction of ocean current and stratification (Vialard et al., 2003), and it can double from one simulation to the other. Fig. 6 suggests that, depending on the time period, RUN-TAO and RUN-SSMI simulate too strong TIWs. The RUN-ERA and RUN-ERS are close to the TMI observations, and RUN-NCEP shows the lowest level of activity. It is probable that the RUN-NCEP weak TIWs intensity is linked to the weak wind stress mean. However, mechanisms determining the TIWs intensity might also be more complex. For example, in the Atlantic Ocean, Athie et al. (submitted for publication) suggested that an artificial high frequency in the NCEP wind forcing interacts destructively with the TIWs and contributes to their intensity decrease. Such a mechanism might also occur in the Pacific Ocean and reduce the TIW activity.

The index presented here characterizes only one aspect of TIWs, and additional analyses have been performed, suggesting that the mechanisms generating TIWs might be different from one simulation to the other. Such a complete analysis and description is however beyond the scope of this paper.

3.4. Preliminary conclusions

From these first analyses, it is obvious that differences in the wind stress products affect the surface and subsurface dynamics and thermodynamics of the simulated ocean. Mean surface currents are almost doubled in the cold tongue from one simulation to the other, and so are TIW intensities. The oceanic response to wind stress forcing is highly non linear. Differences in some oceanic parameters (mean meridional and vertical currents, mean thermocline depth and slope) may be explained simply by differences in wind properties. However, for most of the other parameters (temperature gradients, TIW intensity and generation), it is not possible to find a simple relationship between wind stress and oceanic differences. Therefore, we expect the heat budget terms to be also very different from one simulation to the other, but we do not expect to be able to interpret unambiguously these differences.

Regarding all the comparisons we made between observed and simulated surface and subsurface temperature and currents, we would conclude that the most adequate model wind forcings are TAO, SSMI and ERA-40 and the least adequate is NCEP. While it has been suggested that ERA winds better compare to the observations than NCEP winds in the tropics (Caires et al., 2004) (see also Fig. 1) it would however be premature to conclude about a "best forcing field" as the results are certainly dependent on model physics (mixing, resolution, advection scheme, etc...). Further studies needs to be conducted to explore these aspects more thoroughly.

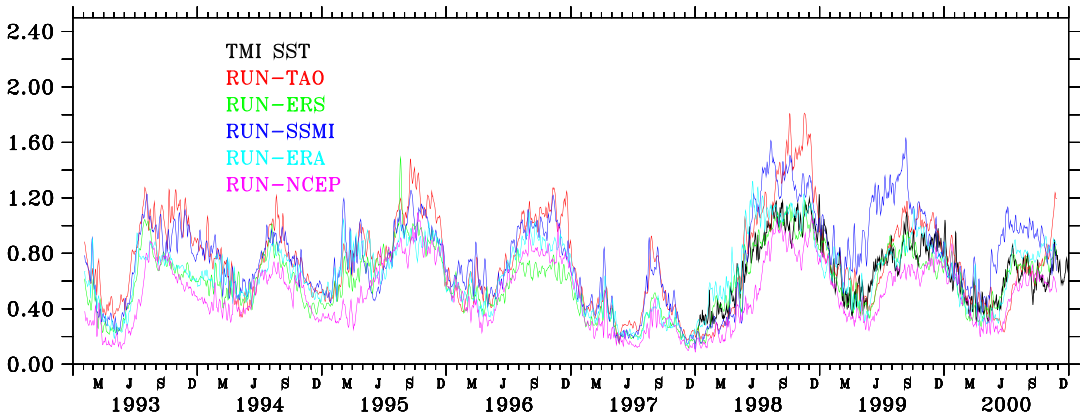

Fig. 6. Index of TIWs activity computed from the five simulations and from TMI SST (thick black line). The index is defined as the spatial root-mean square of high passed SST in the 160–90°W, 0–4°N box. SST are high-passed with a 69-day sparzen filter.

4. Mean heat budget

4.1. The heat budget equation

To understand how oceanic processes and atmospheric forcing participate to the balance and the time evolution of the SST in the cold tongue, the different terms of a mixed layer heat budget are analyzed. A mixed layer budget method (Menkes et al., 2006; Vialard et al., 2001) is used to compute on-line the vertically averaged temperature tendency trends within the time-varying mixed layer depth. We define the base of the mixed layer as the depth where the potential density is higher than the surface density by 0.05 kg m^{-3}. The mixed layer temperature T_{ml} is an excellent proxy for the SST.

The equation for T_{ml} can be written as:

$$\partial_t T_{ml} = \underbrace{\frac{Q - Qs(-h)}{\rho_0.cp.h}}_{A} - \underbrace{\frac{1}{h}\int_{-h}^{0} \overline{\mathbf{u}}.\nabla\overline{\mathbf{T}}}_{B} - \underbrace{\frac{1}{h}\int_{-h}^{0} \mathbf{u}'.\nabla T'}_{C} - \underbrace{\frac{1}{h}\int_{-h}^{0} (\overline{\mathbf{u}}.\nabla\mathbf{T}' + \mathbf{u}'.\nabla\overline{T})}_{C'} - \underbrace{\underbrace{(\partial_t h + w(-h)) \cdot \left(\frac{T_{ml} - T(-h)}{h}\right)}_{D2} + \underbrace{\frac{(K_z\partial_z T)(-h)}{h}}_{D1}}_{D} + \underbrace{\frac{1}{h}\int_{-h}^{0} D(T)dz}_{E} \quad (1)$$

where h is the time-varying depth of the mixed layer, Q is the total surface heat flux, Qs the solar heat flux; $Qs(-h)$ thus represents the fraction of the solar shortwave flux that penetrates through the base of the mixed layer. $\mathbf{u} = (u, v)$ is the horizontal velocity and w the vertical velocity. Temperature and currents are separated offline into a low-frequency component (denoted by a bar) and an eddy component (denoted by a prime). We use a 69-day Sparzen filter to separate the low-frequency part from the eddy part. K_z is the vertical eddy diffusivity coefficient, ρ_0 is the seawater density, and cp the specific heat. The first term in the second member (A, referred to as "atmospheric forcing") thus represents the part of the atmospheric forcing absorbed by the mixed layer. The second one (B, referred to as "mean advection") represents the advection of the low-frequency temperature by the low-frequency currents. The third and fourth terms (C and C', referred to as "eddy advection") represent the effects of eddies: the advection of anomalous temperature by anomalous currents, the advection of anomalous temperature by mean currents and advection of mean temperature by anomalous currents. Term C is by far larger than term C' for the mean. Given the choice of the filter, the eddy part contains all the energy at periods lower than 35 days, and half of the energy at 80 days period. This encompasses not only TIWs but also the higher frequency wind forced variability and a portion of the intraseasonal Kelvin waves. Nevertheless, it was confirmed that TIWs stand out as the dominant signal in the eastern Pacific. It is worth noting that we tried different filters and different frequency bands to isolate the TIWs. Although the choice of the filter type or cut-off period may slightly change the amplitude of the eddy fields, it does not change our results. The term D (referred to as "subsurface") represents the exchanges with the deeper ocean. It includes the entrainment through the base of the mixed layer ($D2$) and the turbulent mixing ($D1$). Finally, the term E (representing the lateral diffusion) is found negligible. For additional details about the contribution of all these terms on the long-term mean and TIW scales, the reader is referred to Menkes et al. (2006).

4.2. The mean 1993–2000 heat budget components

How are the different tendency terms acting to equilibrate the mean SST in the different simulations? To answer this question, we average equation 1, and obtain:

$$\frac{T(t_f) - T(t_i)}{(t_f - t_i)} \approx 0 = \frac{1}{(t_f - t_i)} \int_{t_i}^{t_f} (A(u) + B(u) + C(u) + C'(u) + D(u))du \quad (2)$$

where t_i is the initial time (January, 1st 1993) and t_f is the final time (December, 31st 2000) of the period we wish to study. Each integrated tendency term is examined separately. Fig. 7 presents the respective contributions of the tendency terms determining the mean SST over 1993–2000, in °C per month, averaged in the 160–90°W, 2°S–2°N box that encompasses the cold tongue. The dominant terms contributing to the warming of the cold tongue are the atmospheric forcing (mostly the solar heat flux) and the TIW-induced horizontal advection. Both are of the same order of magnitude. Lateral diffusion is negligible. The terms contributing to the cooling are the exchanges with the subsurface through vertical advection and turbulent mixing (dominant) and the mean advection, notably due to the mean meridional currents that advect warm waters poleward. The mean zonal advection is very small and almost negligible in this region, due to small horizontal SST gradients. It is important though to note that the processes described above are those that redistribute heat inside the cold tongue. When studying the external processes that warm or cool the cold tongue, the balance is slightly different (Kim et al., 2007). Especially, the importance of TIW warming is reduced since a large part of TIW lies within the cold tongue.

These results corroborate the findings of previous studies. More interesting are the quantitative differences of these terms between the different simulations. The smallest values for all terms are found in the RUN-NCEP, where the exchanges with the subsurface contribute to a mean cooling of 2.56 °C/month over the 1993–2000 period (by adding terms $D1$ and $D2$ in Fig. 7), while the eddy advection warms the cold tongue by 1.45 °C/month. In contrast, the strongest values are found in RUN-TAO and RUN-SSMI. For instance, in the RUN-SSMI simulation, the exchanges with the subsurface cool the cold tongue by 4.76 °C/month over the same period, whereas the eddy advection warms the cold tongue by 2.67 °C/month. Therefore, the intensity of the exchanges can be almost doubled from one simulation to the other. This is consistent with the wide variations presented in Liu et al.'s (1996) plate 5 for their SSM/I and ECMWF simulations. To check how these different modelled estimates of the mixed layer heat budget compare to the observations, a comparison with previous studies at TAO moorings locations is presented in Appendix.

What could be the causes of these differences observed in the different simulations? Obviously, this is related to properties of the wind forcing (Fig. 1). Terms A and D in the heat equation (Eq. (1)) are inversely proportional to the depth of the mixed layer. However, the differences in mixed layer depth from one run to another are no greater than 20% (see, for instance, Fig. 8b). Variation in modelled mixed layer depth may thus only explain a small part of the differences in the heat budget terms. Naturally, one would want to pinpoint how the wind differences seen in Fig. 1 and Table 2 translate into the differences in the heat balance numbers seen between our simulations. Differences in wind stress and wind kinetic energy input into the ocean change the mean advection, the turbulent mixing and the temperature stratification. However, as noted in section 3.4, the oceanic response is highly non linear, and it is not possible to relate simply wind stress and heat budget differences.

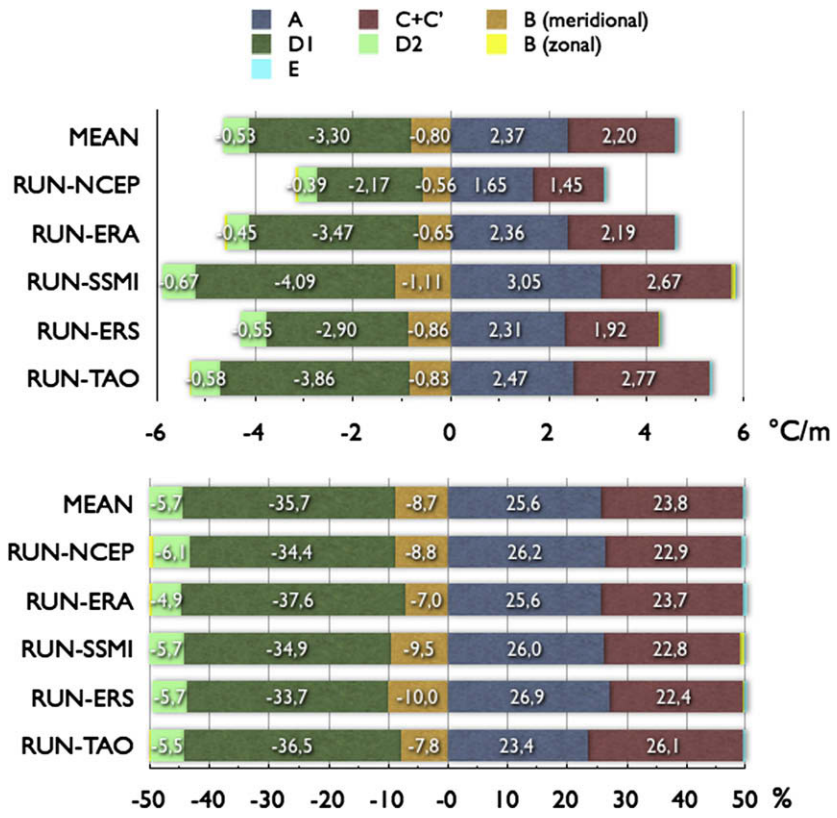

Fig. 7. Mean 1993–2000 SST tendencies for the five simulations, and for their mean, averaged in the 160–90°W, 2°S–2°N box. The atmospheric forcing (A) is in dark blue; the entrainment through the base of the mixed layer ($D2$) is in light green and the turbulent mixing ($D1$) in dark green. The mean zonal advection (part of term B) is in yellow, the mean meridional advection (part of B) in orange, and the advection by the eddies ($C + C'$) in red. Diffusion (E) is in light blue. Top: in °C per month. Bottom, in percentage of the total heat exchanges. Associated numerical values are indicated only when the percentage is higher than 1%. (For interpretation of the references to colour in this figure legend, the reader is referred to the web version of this article.)

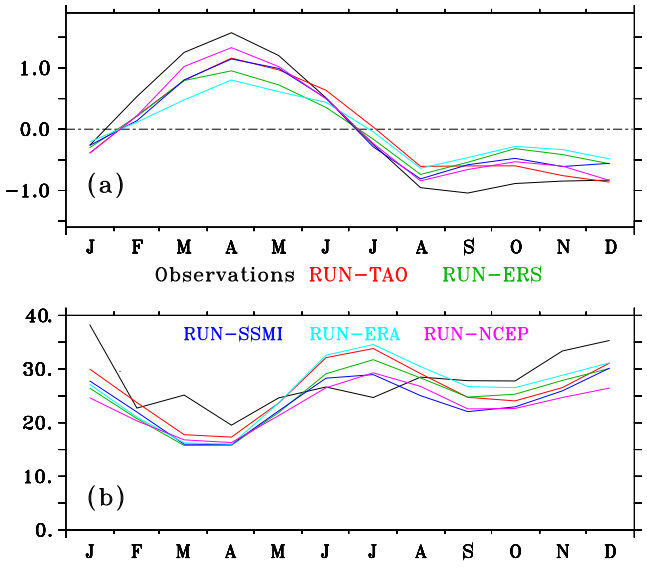

Fig. 8. (a) Mean 1993–2000 SST seasonal cycle, averaged in the 160–90°W, 2°S–2°N box, for the five simulations and for Reynolds SST (thick black line). Annual means have been removed. (b) Mean 1993–2000 MLD seasonal cycle, averaged in the 160–90°W, 2°S-2°N box, for the five simulations and for de Boyer Montegut data (thick black line).

Strikingly, and that is a major result of the study, the same exchanges presented as percentage of the total heat exchanges for each run reveal that, at first order, the dominant processes governing the SST variability are equal in all simulations. Around 41% of the mean cooling is due to exchanges with subsurface (among which 33.7–37.6% is due to turbulent mixing), and around 9% of the mean cooling is due to advection of mean temperature gradients by mean meridional currents. Warming by eddies represent between 22.4% and 26% of the total heat exchanges and atmospheric forcing heating between 23.4% and 27% also. Lateral diffusion and zonal advection represent less than 1% of the total heat exchanges.

These results are quite important since they reveal that the quantitative estimations of the mean heat budget tendencies greatly depend onto the wind forcing and can vary by a factor 2 from one wind forcing to another. On the contrary, whatever the wind forcing used in this study, the contribution of each process to the total SST budget is approximately equal from one simulation to another. Thus, while it is difficult to quantitatively estimate the values of each term contributing to the SST evolution in an ocean model, since it is so dependent on wind forcing, it gives confidence in the repartition of the processes dominating SST evolution on the long-term mean.

4.3. Seasonal heat budget

Fig. 8a shows the mean 1993–2000 SST seasonal cycle for the five simulations and for Reynolds SST data. The SST seasonal cycle amplitude is different from one simulation to the other. Curiously, the RUN-NCEP exhibits the maximum and more realistic SST seasonal amplitude, despite the fact it is too warm throughout the year, and despite the fact that the NCEP wind stress seasonal cycle is weaker. That illustrates again, if needed, how nonlinear the system is in its dynamical and thermodynamical responses to wind

forcing. The mixed layer is shallower (around 15 m depth) in March–April and deeper (around 25–35 m depth) in June–July and December–January (Fig. 8b), in the runs and in data (de Boyer Montegut et al., 2004). These variations closely follow the wind speed variations.

Fig. 9 is the seasonal counterpart of Fig. 7 and confirms at seasonal timescales what Fig. 7 showed for the mean heat budget. In an absolute sense, each quantitative estimate of the processes entering the SST seasonal evolution can be widely different from one run to another (top panel) for the dominating terms. In contrast, differences in the percentage of the contributions to the seasonal SST evolution between all the runs are small (bottom panel). The only notable differences concern the RUN-NCEP, in which the relative contribution of the mean advection cooling to the total heat fluxes exchanges is smaller from January to March (and greater from May to September) than the others, inducing a greater warming from January to March (and a stronger cooling from May to September). Secondly, the atmospheric forcing heats relatively more during January to March in the RUN-NCEP than in the other runs. The combination of increased heat storage due to stronger heat fluxes and weaker low-frequency advective cooling at the beginning of the year results in a higher SST seasonal amplitude in RUN-NCEP compared to the other simulations.

Aside from that difference, panel b allows us to discuss the repartition of the terms constructing the SST seasonal cycle with confidence since all curves from the diverse wind forcings are very similar. During boreal winter, SSTs are warmed by atmospheric heat fluxes (~35%) and cooled by turbulent vertical mixing (~30/35%). Vertical advection and low-frequency advection cool SSTs by about 7–10% each and eddies warm the mixed layer by about 15% (most of which is driven by zonal advection). During that time, TIW activity progressively slows down as the dynamics slows. By May, the dynamics is taking up again and the mixed layer deepens. During boreal autumn, the atmospheric forcing warming accounts for 20% of the total heat fluxes exchanges, reinforced by 30% due to eddies warming. This warming is almost balanced by turbulent cooling (35%), vertical advection (5%) and low-frequency advection (10%). These results confirm what was known about the SST seasonal cycle from previous studies, showing that the oceanic tendency terms mimic the mean seasonal cycle of surface winds strongest during the second half of the year (Kessler et al., 1998). The evolutions on the top panel are qualitatively similar to those found in Vialard et al. (2001) (see their Fig. 10b) although they used a different model grid configuration. However, they are different from those of Kim et al. (2007) who used a boundary flux method applied on a larger box, and who found a negligible TIWs contribution.

These results on the seasonal cycle confirm that the processes that govern the SST evolution at seasonal timescales are qualitatively the same whatever the wind forcing is. However, their amplitude greatly depends of the wind forcing.

4.4. Heat budget during the abrupt cooling in April–August 1998

Do our conclusions for the mean and seasonal heat budget also apply during a particular event, such as the abrupt transition from the 1997 El Niño to the 1998 La Niña? In May 1998, a SST drop of about 5 °C in one month (reaching 8 °C at TAO mooring located at the equator at 125°W) occurred in the eastern Pacific (Fig. 10), bringing suddenly the 1997 El Niño to an end, and establishing La Niña conditions (McPhaden, 1999). This SST drop has been linked to the combination of a progressive shoaling of the thermocline by equatorial upwelling waves (McPhaden and Yu, 1999) until May, and of the reestablishment of the easterlies early May. The easterlies entrained cold waters from the shoaled thermocline that finally outcropped. The amplitude and timing of this drop are correctly simulated in all simulations, though it is much less abrupt in RUN-NCEP than in other simulations (Fig. 10). Note that the RUN-TAO, RUN-SSMI and RUN-NCEP exhibit about the same SST prior to May 1998 and that the RUN-NCEP shows a 1 °C difference with

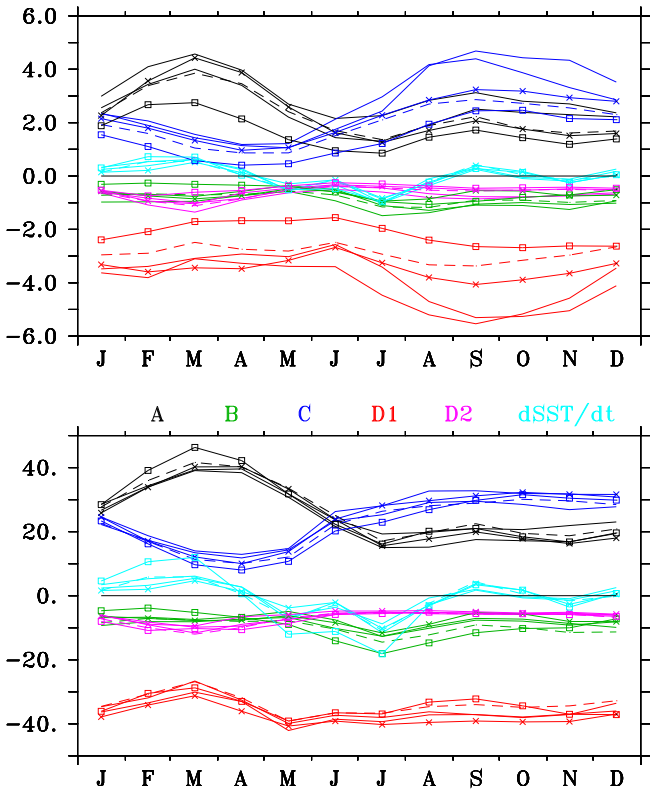

Fig. 9. Mean 1993–2000 seasonal cycle of the SST tendencies, averaged in the 160–90°W, 2°S–2°N box, for the five simulations (RUN-TAO: thick line; RUN-ERS: dashed line; RUN-SSMI: light line; RUN-ERA: line with crosses; RUN-NCEP: line with squares). dSST/dt is in light blue; the atmospheric forcing (A) in black; the entrainment through the base of the mixed layer ($D2$) is in purple and the turbulent mixing ($D1$) in red. The mean advection (B) is in green, and the advection by the eddies ($C + C'$) in dark blue. Top: in °C per month. Bottom : in percentage of the total heat exchanges. (For interpretation of the references to colour in this figure legend, the reader is referred to the web version of this article.)

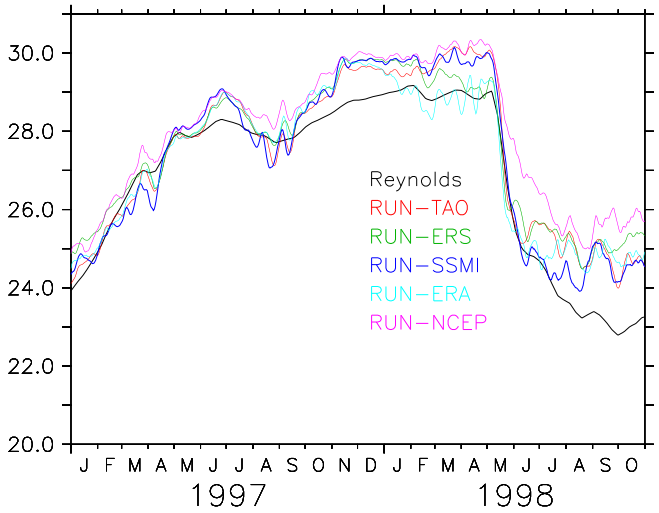

Fig. 10. Observed and simulated SST averaged in the 160–90°W, 2°S–2°N box from January 1997 to October 1998.

these latter runs even by October. To understand these evolutions, we now turn to the SST budget during that period.

Fig. 11 presents the time integrated SST tendency terms in °C for the five simulations, beginning in May 1998. In all simulations, the strong cooling is initiated and explained by a strong turbulent mixing at the base of the mixed layer. The easterlies mix the cold subsurface waters with the warm surface waters. A few days later, vertical and meridional advection (zonal advection tends to warm, but to a lesser extent (not shown)) also contributes to a lesser extend to the cooling, which is counterbalanced by atmospheric fluxes that warm the cold surface waters. Eddies also begin to warm, as the stronger dynamics is taking place again. These mechanisms are coherent with what is known about this cooling: the oceanic processes (mainly in subsurface) dominate the cooling, and the atmospheric fluxes counterbalance it. It is consistent with the results found in another model configuration by Vialard et al. (2001) (see their Fig. 13), and with the findings of Kim et al. (2007) (see their Fig. 15), who used a boundary flux method.

Interestingly, we see from Fig. 11 that the final SST cooling evolution is similar in all runs, and that the processes dominating the SST changes are qualitatively the same while their quantities can greatly differ. For instance, the cumulative turbulent cooling ranges from 3.5 for RUN-NCEP to 8.1 °C for RUN-ERA in 45 days. This may be in part explained by the wind speed differences. In May 1998, the trade winds increased suddenly in all runs, except in RUN-NCEP (not shown). In all runs, the termination of El Niño was preconditioned by an elevation of the thermocline by upwelling waves. Thus in RUN-NCEP, this termination is not reinforced by the trade winds intensification, and the cooling is less sudden. Once the cooling is sufficiently initiated, the atmospheric fluxes act to warm the waters (from 1 for RUN-NCEP to 4.5 °C for RUN-ERA in 45 days). The latent heat flux cooling, weaker in RUN-ERA than in RUN-NCEP, explain the major part of the differences in total atmospheric warming (not shown). The remaining of the differences in atmospheric warming is explained by smaller longwave and sensible cooling in RUN-ERA. As explained in Section 2, heat

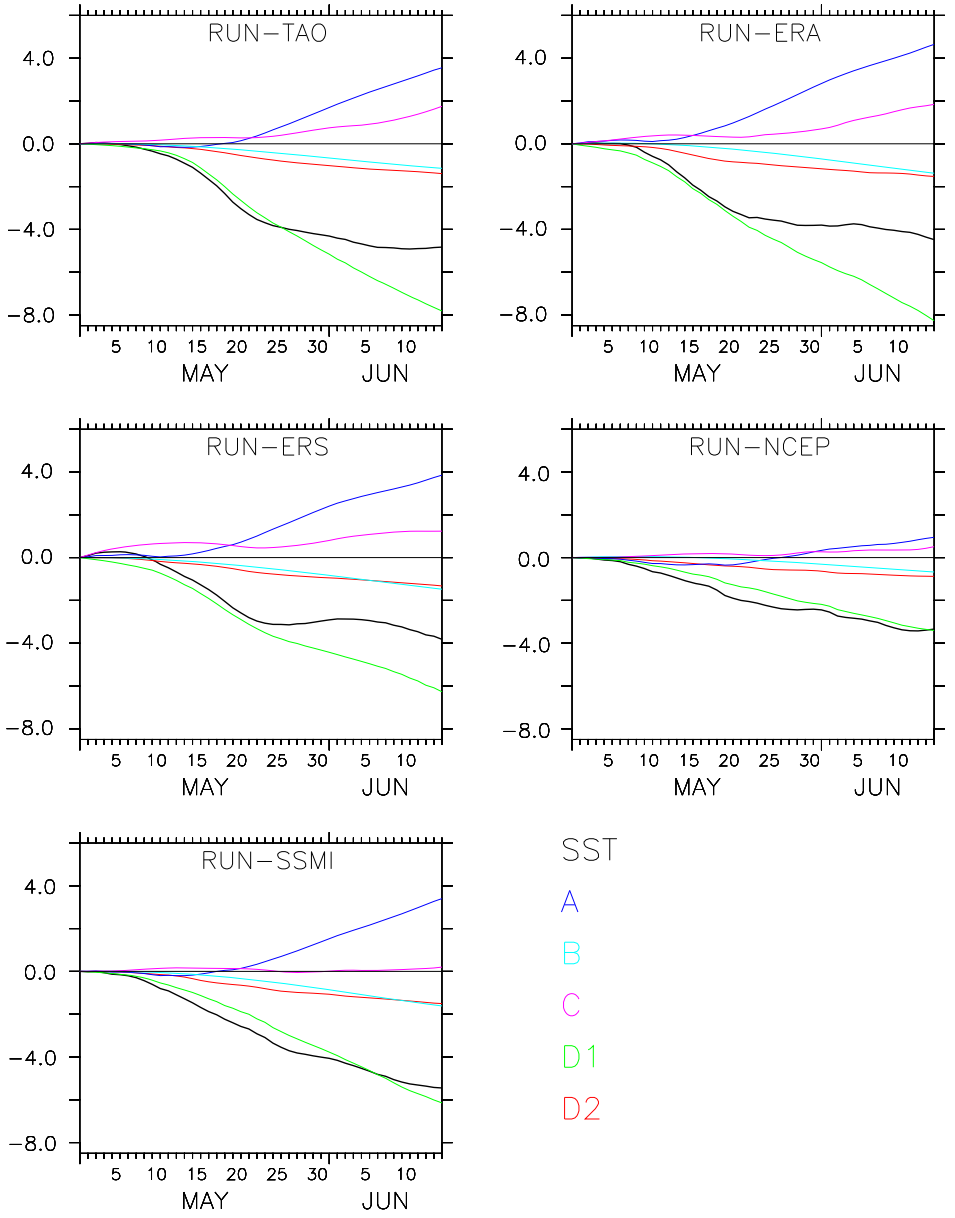

Fig. 11. SST tendencies averaged in the 160–90°W, 2°S–2°N box for the five simulations. The SST tendencies curves are time integrals from 1st May 1998 to 15th June 1998, and units are in °C. In each panel, the thick black line represents the SST evolution from 1st May 1998.

fluxes are computed using bulk formulae, using the NCEP winds and the simulated SST. This introduces a sort of relaxation term, and the heat gains are thus totally controlled by the SST differences in the runs. The stronger the cooling by turbulent mixing is, the stronger the SST decrease is, and the stronger the counterbalancing warming by atmospheric fluxes is. Differences in the eddy warming contributions arise from the differences in the timing of TIWs reappearance. Weaker easterlies also explain weaker cooling by mean advection. However, these small differences in the relative contributions of the different terms to the heat budget do not alter the fact that the main processes contributing to this important drop are qualitatively the same, whatever the wind forcing is, at least among the five used in this study.

5. Discussion and implications

In this paper, we utilized a commonly used state-of-the-art climate-type OGCM, ORCA2, that had been heavily validated against observations in terms of sea level, heat content, vertical temperature, current structure and water mass properties (http://www.nemo-ocean.eu/superbib/en/one/superbib01.html). Here, we quantified the sensitivity of the cold tongue oceanic heat budget to five different wind forcing. We showed that the different components of the oceanic heat budget are quantitatively greatly affected by the choice of the wind forcing. This had been suggested in a preliminary study by Liu et al. (1996), using another ocean model, and using two wind stress data sets from ECMWF and SSM/I for another time period. This result does not come as a surprise but it does give a humble perspective on the validity of the quantitative estimates of upper ocean heat budgets (here, the mixed layer budget) in such model validations: the amplitude of the terms explaining SST variations can double from one simulation to the other.

Notwithstanding, the relative contributions of the terms, i.e. TIW advection, mean advection, atmospheric forcing and mixing at the base of the mixed layer are the same in all simulations forced by the different wind stress products used in this study, for the mean 1993–2000 period and at seasonal timescales. They are also very similar in more extreme events such as during the abrupt cooling observed in the cold tongue in May 1998. Therefore, this paper suggests that model users must be very cautious when estimating quantitatively heat budgets terms with one simulation only. We would argue that without such sensitivity, one cannot claim to reach correct quantitative estimates. However, we suggest that they can be confident, within their model configurations, in the relative contributions of the processes governing the heat budget, whatever the wind stress product used to force their model is.

It is worth noting though that this paper does not pretend to be a fully comprehensive study on the heat budget dependence to the wind forcing. It is limited to five wind products, and we cannot be absolutely certain that our results would hold with another wind forcing. Our study is also limited to a specific region, the Pacific cold tongue. It is not sure that our results could be extrapolated to other areas, such as the Warm Pool region. Moreover, our experimental setup consists on a highly constrain system by using bulk formulae. Our results probably would not hold in a coupled system. Finally, our study is limited to a model configuration. Naturally, one can wonder how the previous consideration holds from a model configuration to another one. To somewhat answer this question, we took the RE3-TDH experiment of Menkes et al. (2006). The main differences between the ORCA2 and the TDH experiments lie in the configuration (TDH is a closed Pacific domain unlike the ORCA2 global configuration), and in the horizontal resolution (in TDH, the zonal resolution is half of that of ORCA2). It also lie in the different advection numerical scheme, which does somehow impact the zonal currents and the Tropical Cells as discussed in Cravatte et al. (2007), and in the heat fluxes (in TDH, they are calculated from an ECMWF climatology). The momentum forcing is the same than in RUN-TAO. We repeated on Fig. 12 the calculations performed on Fig. 7 but on a common period 1993–1996 and compared to RUN-TAO for reference. While the quantitative values again vary widely from one configuration to another, the percentage of the contribution of each process in the total heat exchanges are very similar. This result gives us confidence in the partition of the processes in the total heat exchanges independently of winds and model configurations, within the OPA framework. The remaining question is whether that holds in models of very different physics such as isopycnal or terrain-following coordinate model, or with different mixed layer physics.

Finally, from our results shown in section 3, one would conclude that the most adequate model wind forcings for our model's ability to simulate reality are TAO and ERA40, SSM/I and the least adequate is NCEP. NCEP and ERA-40 reanalyses are often used because of their long and valuable time series. It is worth pointing out that the choice of reanalyses product forcing is crucial to study decadal variability. Decadal variability of the mean state of the tropical Pacific is suspected to influence ENSO characteristics, and a variation of 0.5–1 °C is observed in the eastern Pacific at dec-

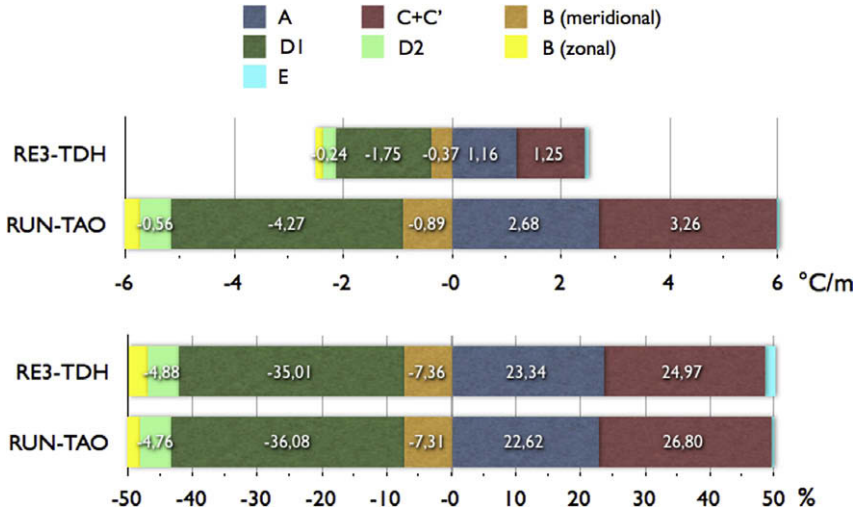

Fig. 12. Same as Fig. 6 for the mean 1993–1996 SST tendency terms for RUN-TAO and RE3-TDH simulation (see text).

adal timescales, similar to the mean SST differences in RUN-NCEP and RUN-ERA. Moreover, with the atmospheric fluxes parameterized with bulk formulae, the SST in the cold tongue cannot diverge too much between the runs. Other oceanic parameters may be much more sensitive to the different physical oceanic processes produced by the different wind forcings. Preliminary results show that differences in the wind forcing are indeed further amplified in biological models. The phytoplankton bloom observed in June 1998 (Ryan et al., 2002), prominent in RUN-TAO, is nonexistent in RUN-NCEP when coupling ORCA to the PISCES (Aumont and Bopp, 2006) biological model. It is thus necessary, as did Rodgers et al. (2008) who looked at biological shifts in ORCA/PISCES forced by NCEP/NCAR reanalyses, to confirm model results using ERA40 reanalyses.

This advocates, as we have tried to do in that study, for the use of multiple wind forcings when dealing with issues as uncertain as heat and momentum budgets, and even more for biological budgets such as primary production or carbon budgets in coupled dynamical–biogeochemical models.

Acknowledgments

The authors acknowledge the use of freely available wind stress products for this study. ERS wind fields were provided by CERSAT/IFREMER (Institut Français de Recherche pour l'Exploitation de la Mer). SSMI/I winds data were downloaded from (ftp://podaac.jpl.nasa.gov/pub/ocean_wind/ssmi/atlas_ssmi_ver10/data/level 3.5_5day). They also wish to acknowledge Dr Lumpkin who kindly provided the drifter-derived climatology of global near-surface currents. These currents were obtained from (http://www.aoml.noaa.gov/phod/dac/drifter_climatology.html). They wish to thank IDRIS for calculation time, and to acknowledge the kindness and constant help from the OPA team and Gurvan Madec in particular. They also thank T. Delcroix, G. Alory and two anonymous reviewers for useful comments on this study. The authors finally wish to acknowledge use of the Ferret program for analysis and graphics in this paper. Ferret is a product of NOAA's Pacific Marine Environmental Laboratory (Information is available at http://ferret.pmel.noaa.gov/Ferret/.).

This work was supported by CNRS (Centre National de la Recherche Scientifique) and IRD (Institut de Recherche pour le Développement).

Appendix A

How do our SST budget estimates compare to data? To answer this question, table 3 compares our estimates of the mean heat budget tendencies from the mean of our five runs to those of Wang and McPhaden (1999) (WMP99) and Jochum et al. (2007) who used TAO moorings data located in the cold tongue. It shows a comparison for atmospheric forcing, for total zonal and meridional advection (to allow the comparison with WMP99), separately for advection by eddies (to allow the comparison with Jochum et al. (2007)), and for subsurface tendencies at 140 and 110°W equatorial moorings. Our model overestimates all tendency terms. In particular, large discrepancies can be observed between our modelled estimates of warming by atmospheric forcing and cooling by subsurface processes and those estimated by WMP99. The modelled estimates are 2–3 times larger than the WMP99 estimates. Several reasons may explain these differences. The first one is the way the mixed layer depth is defined. Terms A and D in the heat equation are inversely proportional to the mixed layer depth. In WMP99, the mixed layer depth is defined as the depth at which the temperature is 0.58 °C lower than the SST. Seasonally, it varies between 30 and 65 m at 140°W, and between 15 and 30 m at 110°W. In our model, it is estimated as the depth at which the density is smaller than the surface density by 0.05 kg m^{-3}. Seasonally, it varies between 12 and 28 m at 140°W, and between 10 and 14 m at 110°W, values that compare reasonably with observations based on similar criteria (see Fig. 8b). Therefore, the mixed layer depth used to compute the heat budget equation is 2–3 times shallower in our model (and in de Boyer Montegut et al.'s, 2004 data) than in WMP99 observations. This may explain a significant part of the differences in atmospheric forcing and subsurface processes tendencies.

All our simulations show a strong contribution of eddy horizontal advection in the SST budget, a conclusion reached also by Jochum et al. (2007). This is at odds with WMP99's conclusion at 110 and 140°W where zonal advection is very different from our model simulations. In this case, as suggested by Vialard et al. (2001) and shown by Jochum et al. (2007), we incriminate the data used by WMP99 to calculate this advection term. Indeed, they used Reynolds weekly SSTs to calculate gradients at the TAO moorings while it is very important to use high space/time resolution SSTs coincident with the currents to resolve the scales associated with TIWs as shown in Jochum et al. (2007). Indeed, zonal eddy advection is dominated by the eddy temperature–eddy current interaction (Menkes et al.'s (2006)'s Fig. 5d) in constrast to the meridional advection terms where the contribution of the eddy meridional current acting on the mean temperature meridional gradient is important (Menkes et al. (2006)'s Fig. 5h). Thus using Reynolds SSTs as in WMP99 allow to qualitatively estimating the eddy induced meridional advection but not the eddy-induced zonal advection, thus allowing zonal advection by the SEC (weaker, and of opposite sign) to dominate the zonal advection budget.

Lastly, Jochum et al. (2007) estimated the role of eddy zonal advection both from observations and a model (Table 3). At 140°W, both our and their model agree on the zonal advection warming, by contrast to the observations from their table. Aside from these, the two models show similar warming behaviour by eddies but globally overestimate the eddy warming deduced from observations.

Finally, it is hard to really compare all these estimates, as the time period of the computation for each dataset is different. It

Table 3
Estimates of mean atmospheric forcing, total zonal and meridional advection, zonal and meridional advection due to eddies and subsurface tendency contributions to the SST budget. Estimates are given for the mean and standard deviation of the five runs for the 1993–2000 period, and for Wang and McPhaden (1999) and Jochum et al. (2007) studies. The estimates are given at two TAO moorings locations in the eastern part of the basin. Units are °C per month.

	Model	Wang and McPhaden (1999)	Jochum et al. (2007)
Atmospheric forcing			
140°W	2.49 ± 0.35	0.75 ± 0.28	
110°W	4.41 ± 0.74	1.91 ± 0.56	
Total zonal advection			
140°W	0.45 ± 0.30	−0.01 ± 0.17	
110°W	1.47 ± 0.41	−0.17 ± 0.22	
Total meridional advection			
140°W	1.53 ± 0.33	0.90 ± 0.17	
110°W	2.20 ± 0.37	1.50 ± 0.21	
$-T'U'$			
140°W	0.46 ± 0.32		−0.07 ± 0.30
110°W	1.47 ± 0.41		0.69 ± 0.47
$-T'V'$			
140°W	2.33 ± 0.52		0.82 ± 0.41
110°W	3.00 ± 0.54		2.09 ± 0.89
Subsurface			
140°W	−4.66 ± 0.73	−1.63 ± 0.26	
110°W	−8.35 ± 1.37	−3.22 ± 0.78	

may induce changes in the processes governing the SST. In particular, 2 El Niño events occur during the period chosen by Jochum et al. (2007) to estimate the temperature advection by tropical instability waves, whose intensity is greatly reduced during El Niño years.

To conclude, the mixed layer criterion, the period chosen, and the way the different heat budget tendency terms are computed are different in the data and in the simulations. Therefore, it seems quite impossible to compare our simulated estimates with those from WMP99 and Jochum et al. (2007), quantitatively and even qualitatively by estimating percentages of total heat exchanges.

References

Agarwal, N., Sharma, R., Basu, S.K., Sarkar, A., Agarwal, V.K., 2007. Evaluation of relative performance of QuikSCAT and NCEP re-analysis winds through simulations by an OGCM. Deep-Sea Research Part I: Oceanographic Research Papers 54 (8), 1311–1328.

Athie, G., Marin, F., Treguier, A.-M., Bourles, B., Guiavarc'h, C., submitted for publication. Sensitivity of near-surface Tropical Instability Waves to submonthly wind forcing in the tropical Atlantic. Ocean Modelling.

Atlas, R., Bloom, S.C., Hoffman, R.N., Brin, E., Ardizzone, J., Terry, J., Bungato, D., Jusem, J.C., 1999. Geophysical validation of NSCAT winds using atmospheric data and analyses. Journal of Geophysical Research: Oceans 104 (C5), 11405–11424.

Aumont, O., Bopp, L., 2006. Globalizing results from ocean in situ iron fertilization studies. Global Biogeochemical Cycles 20 (2).

Ayina, L.H., Bentamy, A., Mestas-Nunez, A.M., Madec, G., 2006. The impact of satellite winds and latent heat fluxes in a numerical simulation of the tropical Pacific Ocean. Journal of Climate 19 (22), 5889–5902.

Baturin, N.G., Niiler, P.P., 1997. Effects of instability waves in the mixed layer of the equatorial Pacific. Journal of Geophysical Research 102 (27), 771–772.

Bentamy, A., Quilfen, Y., Gohin, F., Grima, N., Lenaour, M., Servain, J., 1996. Determination and validation of average wind fields from ERS-1 scatterometer measurements. The Global Atmosphere and Ocean System 4 (1), 1–29.

Blanke, B., Delecluse, P., 1993. Variability of the tropical Atlantic Ocean Simulated by a General Circulation Model with 2 different mixed layer physics. Journal of Physical Oceanography 23 (7), 1363–1388.

Boulanger, J.P., Menkes, C., 2001. The Trident Pacific model. Part 2: role of long equatorial wave reflection on sea surface temperature anomalies during the 1993–1998 TOPEX/POSEIDON period. Climate Dynamics 17 (2–3), 175–186.

Brown, J.N., Fedorov, A.V., 2008. Mean energy balance in the tropical Pacific Ocean. Journal of Marine Research 66 (1), 1–23.

Bryden, H.L., Brady, E.C., 1985. Diagnostic model of the three-dimensional circulation in the upper equatorial Pacific Ocean. Journal of Physical Oceanography 15 (10), 1255–1273.

Bryden, H.L., Brady, E.C., 1989. Eddy momentum and heat fluxes and their effects on the circulation of the equatorial Pacific Ocean. Journal of Marine Research 47, 55–79.

Busalacchi, A.J., Atlas, R.M., Hackert, E.C., 1993. Comparison of Special Sensor Microwave Imager vector wind stress with model-derived and subjective products for the Tropical Pacific. Journal of Geophysical Research: Oceans 98 (C4), 6961–6977.

Caires, S., Sterl, A., Bidlot, J.R., Graham, N., Swail, V., 2004. Intercomparison of different wind-wave reanalyses. Journal of Climate 17 (10), 1893–1913.

Contreras, R.F., 2002. Long-term observations of tropical instability waves. Journal of Physical Oceanography 32 (9), 2715–2722.

Cravatte, S., Madec, G., Izumo, T., Menkes, C., Bozec, A., 2007. Progress in the 3-D circulation of the eastern equatorial Pacific in a climate ocean model. Ocean Modelling 17 (1), 28–48.

de Boyer Montegut, C., Madec, G., Fischer, A.S., Lazar, A., Iudicone, D., 2004. Mixed layer depth over the global ocean: an examination of profile data and a profile-based climatology. Journal of Geophysical Research: Oceans 109 (C12).

Dutrieux, P., Menkes, C.E., Vialard, J., Flament, P., Blanke, B., 2008. Lagrangian study of tropical instability vortices in the Atlantic. Journal of Physical Oceanography 38 (2), 400–417.

Enfield, D.B., 1986. Zonal and seasonal variations of the near-surface heat balance of the equatorial Pacific Ocean. Journal of Physical Oceanography 16 (6), 1038–1054.

Fu, L.L., Chao, Y., 1997. The sensitivity of a global ocean model to wind forcing: a test using sea level and wind observations from satellites and operational wind analysis. Geophysical Research Letters 24 (14), 1783–1786.

Goose, H., 1997. Modelling the large-scale behaviour of the coupled ocean–sea–ice system, Ph.D. Thesis, Université Catholique de Louvain, Louvain la Neuve, Belgium, p. 231.

Grima, N., Bentamy, A., Katsaros, K., Quilfen, Y., Delecluse, P., Levy, C., 1999. Sensitivity of an oceanic general circulation model forced by satellite wind stress fields. Journal of Geophysical Research: Oceans 104 (C4), 7967–7989.

Hackert, E.C., Busalacchi, A.J., Murtugudde, R., 2001. A wind comparison study using an ocean general circulation model for the 1999–1998 El Nino. Journal of Geophysical Research: Oceans 106 (C2), 2345–2362.

Hansen, D.V., Paul, C.A., 1984. Genesis and effects of long waves in the equatorial Pacific. Journal of Geophysical Research 89 (C14), 10431–10440.

Hayes, S.P., Chang, P., McPhaden, M.J., 1991. Variability of the sea surface temperature in the eastern equatorial Pacific during 1986–1988. Journal of Geophysical Research 96 (C6), 10553–10566.

Izumo, T., 2005. The equatorial undercurrent, meridional overturning circulation, and their roles in mass and heat exchanges during El Nino events in the tropical Pacific Ocean. Ocean Dynamics 55 (2), 110–123.

Jiang, C., Thompson, L., Kelly, K.A., 2008. Equatorial influence of QuikSCAT winds in an isopycnal ocean model compared to NCEP2 winds. Ocean Modelling 24 (1–2), 65–71.

Jochum, M., Murtugudde, R., Ferrari, R., Malanotte-Rizzoli, P., 2005. The impact of horizontal resolution on the tropical heat budget in an Atlantic Ocean model. Journal of Climate 18 (6), 841–851.

Jochum, M., Murtugudde, R., 2006. Temperature advection by tropical instability waves. Journal of Physical Oceanography 36 (4), 592–605.

Jochum, M., Cronin, M.F., Kessler, W.S., Shea, D., 2007. Observed horizontal temperature advection by tropical instability waves. Geophysical Research Letters 34 (9), 1.

Kalnay, E., Kanamitsu, M., Kistler, R., Collins, W., Deaven, D., Gandin, L., Iredell, M., Saha, S., White, G., Woollen, J., Zhu, Y., Chelliah, M., Ebisuzaki, W., Higgins, W., Janowiak, J., Mo, K.C., Ropelewski, C., Wang, J., Leetmaa, A., Reynolds, R., Jenne, R., Joseph, D., 1996. The NCEP/NCAR 40-year reanalysis project. Bulletin of the American Meteorological Society 77 (3), 437–471.

Karnauskas, K.B., Murtugudde, R., Busalacchi, A.J., 2007. The effect of the Galapagos Islands on the equatorial Pacific cold tongue. Journal of Physical Oceanography 37 (5), 1266–1281.

Kennan, S.C., Flament, P.J., 2000. Observations of a tropical instability vortex. Journal of Physical Oceanography 30 (9), 2277–2301.

Kessler, W.S., Rothstein, L.M., Chen, D.K., 1998. The annual cycle of SST in the eastern tropical Pacific, diagnosed in an ocean GCM. Journal of Climate 11 (5), 777–799.

Kessler, W.S., Johnson, G.C., Moore, D.W., 2003. Sverdrup and nonlinear dynamics of the Pacific equatorial currents. Journal of Physical Oceanography 33 (5), 994–1008.

Kim, S.B., Lee, T., Fukumori, I., 2007. Mechanisms controlling the interannual variation of mixed layer temperature averaged over the Nino-3 region. Journal of Climate 20 (15), 3822–3843.

Kistler, R., Kalnay, E., Collins, W., Saha, S., White, G., Woollen, J., Chelliah, M., Ebisuzaki, W., Kanamitsu, M., Kousky, V., van den Dool, H., Jenne, R., Fiorino, M., 2001. The NCEP-NCAR 50-year reanalysis: monthly means CD-ROM and documentation. Bulletin of the American Meteorological Society 82 (2), 247–267.

Legeckis, R., 1977. Long waves in the eastern equatorial Pacific Ocean: a view from a geostationnery satellite. Science 197, 1179–1181.

Lengaigne, M., Madec, G., Menkes, C., Alory, G., 2003. Impact of isopycnal mixing on the tropical ocean circulation. Journal of Geophysical Research-Oceans 108 (C11).

Levitus, S., 1998. NODC World Ocean Atlas data, report, NOAA-CIRES Clim. Diag. Cent., Boulder, Colorado.

Levy, M., Estublier, A., Madec, G., 2001. Choice of an advection scheme for biogeochemical models. Geophysical Research Letters 28 (19), 3725–3728.

Liu, W.T., Tang, W.Q., Atlas, R., 1996. Responses of the tropical Pacific to wind forcing as observed by spaceborne sensors and simulated by an ocean general circulation model. Journal of Geophysical Research-Oceans 101 (C7), 16345–16359.

Lumpkin, R., Garraffo, Z., 2005. Evaluating the decomposition of tropical Atlantic drifter observations. Journal of Atmospheric and Oceanic Technology 22 (9), 1403–1415.

Lyman, J.M., Chelton, D.B., deSzoeke, R.A., Samelson, R.M., 2005. Tropical instability waves as a resonance between equatorial Rossby waves. Journal of Physical Oceanography 35 (2), 232–254.

Madec, G., Delecluse, P., Imbard, M., Levy, C., 1998. OPA 8.1 Ocean General Circulation Model reference manual, Notes du Pôle de Modélisation de l'IPSL, vol. 11, 91pp.

McPhaden, M.J., 1999. Genesis and evolution of the 1997–98 El Nino. Science 283 (5404), 950–954.

McPhaden, M.J., Yu, X., 1999. Equatorial waves and the 1997–98 El Nino. Geophysical Research Letters 26 (19), 2961–2964.

Menkes, C., Boulanger, J.-P., Busalacchi, A.J., Vialard, J., Delecluse, P., McPhaden, M.J., Hackert, E., Grima, N., 1998. Impact of TAO vs. ERS wind stresses onto simulations of the tropical Pacific Ocean during the 1993–1998 period by the OPA OGCM, Climatic Impact of Scale Interactions for the Tropical Ocean–Atmosphere System, Euroclivar Workshop Report, Eucliv 13, December 1998, pp. 46–48.

Menkes, C.E., Kennan, S.C., Flament, P., Dandonneau, Y., Masson, S., Biessy, B., Marchal, E., Eldin, G., Grelet, J., Montel, Y., Morliere, A., Lebourges-Dhaussy, A., Moulin, C., Champalbert, G., Herbland, A., 2002. A whirling ecosystem in the equatorial Atlantic. Geophysical Research Letters 29 (11).

Menkes, C.E.R., Vialard, J.G., Kennan, S.C., Boulanger, J.P., Madec, G.V., 2006. A modeling study of the impact of tropical instability waves on the heat budget of the eastern equatorial Pacific. Journal of Physical Oceanography 36 (5), 847–865.

Milliff, R.F., Large, W.G., Morzel, J., Danabasoglu, G., Chin, T.M., 1999. Ocean general circulation model sensitivity to forcing from scatterometer winds. Journal of Geophysical Research-Oceans 104 (C5), 11337–11358.

Paulson, C.A., Simpson, J.J., 1977. Irradiance Measurements in upper Ocean. Journal of Physical Oceanography 7 (6), 952–956.
Pezzi, L.P., Richards, K.J., 2003. Effects of lateral mixing on the mean state and eddy activity of an equatorial ocean. Journal of Geophysical Research-Oceans 108 (C12).
Rodgers, K.B., Aumont, O., Menkes, C., Gorgues, T., 2008. Decadal variations in equatorial Pacific ecosystems and ferrocline/pycnocline decoupling. Global Biogeochemical Cycles 22 (2).
Roullet, G., Madec, G., 2000. Salt conservation, free surface, and varying levels: a new formulation for ocean general circulation models. Journal of Geophysical Research-Oceans 105 (C10), 23927–23942.
Ryan, J.P., Polito, P.S., Strutton, P.G., Chavez, F.P., 2002. Unusual large-scale phytoplankton blooms in the equatorial Pacific. Progress in Oceanography 55 (3–4), 263–285.
Shchepetkin, A.F., McWilliams, J.C., 2005. The regional oceanic modeling system (ROMS): a split-explicit, free-surface, topography-following-coordinate oceanic model. Ocean Modelling 9 (4), 347–404.
Stevenson, J.W., Niiler, P.P., 1983. Upper Ocean heat budget during the Hawaii-to-Tahiti shuttle experiment. Journal of Physical Oceanography 13 (10), 1894–1907.
Swenson, M.S., Hansen, D.V., 1999. Tropical Pacific Ocean mixed layer heat budget: the Pacific cold tongue. Journal of Physical Oceanography 29 (1), 69–81.
Uppala, S.M., Kallberg, P.W., Simmons, A.J., Andrae, U., Bechtold, V.D., Fiorino, M., Gibson, J.K., Haseler, J., Hernandez, A., Kelly, G.A., Li, X., Onogi, K., Saarinen, S., Sokka, N., Allan, R.P., Andersson, E., Arpe, K., Balmaseda, M.A., Beljaars, A.C.M., 2005. L. Van De Berg, J. Bidlot, N. Bormann, S. Caires, F. Chevallier, A. Dethof, M. Dragosavac, M. Fisher, M. Fuentes, S. Hagemann, E. Holm, B. J. Hoskins, L. Isaksen, P. Janssen, R. Jenne, A. P. McNally, J. F. Mahfouf, J. J. Morcrette, N. A. Rayner, R. W. Saunders, P. Simon, A. Sterl, K. E. Trenberth, A. Untch, D. Vasiljevic, P. Viterbo and J. Woollen, The ERA-40 re-analysis. Quarterly Journal of the Royal Meteorological Society 131 (612), 2961–3012.
Vialard, J., Menkes, C., Boulanger, J.P., Delecluse, P., Guilyardi, E., McPhaden, M.J., Madec, G., 2001. A model study of oceanic mechanisms affecting equatorial Pacific sea surface temperature during the 1997–98 El Nino. Journal of Physical Oceanography 31 (7), 1649–1675.
Vialard, J., Menkes, C., Anderson, D.L.T., Balmaseda, M.A., 2003. Sensitivity of Pacific Ocean tropical instability waves to initial conditions. Journal of Physical Oceanography 33 (1), 105–121.
Wang, W.M., McPhaden, M.J., 1999. The surface-layer heat balance in the equatorial Pacific Ocean. Part I: Mean seasonal cycle. Journal of Physical Oceanography 29 (8), 1812–1831.
Wang, W.M., McPhaden, M.J., 2000. The surface-layer heat balance in the equatorial Pacific Ocean. Part II: Interannual variability. Journal of Physical Oceanography 30 (11), 2989–3008.
Wang, W.M., McPhaden, M.J., 2001a. Surface layer temperature balance in the equatorial Pacific during the 1997–98 El Nino and 1998–99 La Nina. Journal of Climate 14 (16), 3393–3407.
Wang, W.M., McPhaden, M.J., 2001b. What is the mean seasonal cycle of surface heat flux in the equatorial Pacific? Journal of Geophysical Research-Oceans 106 (C1), 837–857.
Wentz, F.J., Gentemann, C., Smith, D., Chelton, D., 2000. Satellite measurements of sea surface temperature through clouds. Science 288 (5467), 847.
Xie, P.P., Arkin, P.A., 1996. Analyses of global monthly precipitation using gauge observations, satellite estimates, and numerical model predictions. Journal of Climate 9 (4), 840–858.
Zalesak, S.T., 1979. Fully multidimensional flux-corrected transport algorithms for fluids. Journal of Computational Physics 31 (3), 335–362.